Geoscience Letters

RESEARCH LETTER Open Access

Oil spill discrimination of multi-time-domain shipborne radar images using active contour model

Jin Xu[1], Xinxiang Pan[1], Xuerui Wu[2,3,4*], Baozhu Jia[1], Juan Fei[5], Haixia Wang[6], Bo Li[7] and Can Cui[8]

Abstract

Accidental oil spills cause serious pollution to the ocean and are difficult to control in short time. It is an important guarantee for emergency disposal to effectively monitor oil spills. Remote sensing is the main means to monitor oil spills. High false alarm rate has been an important bottleneck of this technology. In this paper, a multi-time-domain shipborne radar images discrimination mechanism was proposed. Based on the improved Sobel operator, Otsu and linear interpolation, the co-frequency interference noises were detected and suppressed. Gray intensity correction model (GICM) and dual-threshold method were used to eliminate highlighted continuous pixels. Oil films were extracted by using an active contour model (ACM). Finally, a multi-time-domain discrimination mechanism based on variation range tolerance of identified oil films centroids was designed to reduce the false alarm rate. It can provide technical support for decision-making and emergency response.

Keywords: Oil spill, Shipborne radar, Active contour model, Multi-time-domain

Introduction

Oil activities grow rapidly with the development of massive offshore infrastructures for exploration, drilling, transportation, storage, processing and delivery (Maamar et al. 2020; Yuan et al. 2020). Oil spillages caused by many critical steps can damage the marine environment and disrupt the health and economy of coastal communities seriously. Much of oil spills resided at the surface of the ocean (Novelli et al. 2020), having a very long-term harmfulness (Soares et al. 2020; Magris and Giarrizzo 2020; Villalonga et al. 2020; Colvin et al. 2020; Yim et al. 2017). In 2010, the Macondo deep-sea well blowout, commonly known as the *Deepwater Horizon* disaster, caused an estimated 507 million liters of crude oil spill into the Gulf of Mexico (U.S. District Court for the Eastern District of Louisiana 2010). The *Deepwater Horizon* event was widely reported for several months, beginning with coverage of the burning oil rig, the death and injury of the workers, and later the hard work of cleanup and the destruction of ecosystem (Vickner 2020).

Oil spill prevention and response operations cover multiple stages, including spill occurrence, spill monitoring, decision-making and emergency response (Ye et al. 2020). Among them, rapid and effective oil spill monitoring is an auxiliary means to make decision and prevent the further spread of pollution (Li et al. 2020). Oil spill detection ability based on remote sensing images is important in marine environmental monitoring. The development of spaceborne oil spill monitoring technology is relatively mature (Zhou et al. 2020; Zeng and Wang 2020; Zhang et al. 2020; Chen et al. 2010; Eronat 2020). It is difficult for spaceborne sensors to quickly and repeatedly collect information in specified position. It is hard to judge the exact oil spills from a single data in an acquisition cycle. With the emergence of unmanned aerial vehicle (UAV), airborne oil spill monitoring technology developed rapidly (Liu et al. 2019a, b; Chen and Lu 2017). UAV,

*Correspondence: xrwu@shao.ac.cn
[2] School of Resources, Environment and Architectural Engineering, Chifeng University, Chifeng, Inner Mongolia, China
Full list of author information is available at the end of the article

which can carry a variety of equipments hovering for continuous observation, is an important platform of oil spill monitoring in the future. Anti-wind, anti-rain and anti-snow performances are the important bottlenecks of UAV to break through. Shipborne sensors can overcome the severe weather and obtain the images quickly and repeatedly at the accident scene. Shipborne radar has ability of large-range detection in real-time with a wide application prospect in the field of oil spill monitoring. Its ability of detecting oil spills from the echo images have been demonstrated since 1988 (Tennyson 1988; Atanassov et al. 1991), but progress slowly. In recent years, the related achievements have gradually increased (Zhu et al. 2015; Xu et al. 2019a, b; Liu et al. 2019a, b).

False oil films often appear in shipborne radar monitoring, which will lead to error alarm and waste various emergency resources. In this paper, based on multi-time-domain continuous acquisition of shipborne radar images, a comprehensive discrimination mechanism was proposed for the correct judgment of oil spills to reduce the false alarm rate. In our case analysis, an improved Local Binary Fitting (LBF) model (Xu et al. 2019a, b) was used to extract oil films from shipborne radar images. The remainder of this paper is composed as follows: "Materials and methods" section presents experimental images and theoretical methods. The experimental results are shown in "Results" section. The discussion and comparisons are expounded in "Discussion" section. The last part is the conclusion.

Materials and methods

Dataset

According to our requirements, a set of shipborne radar images (Fig. 1) collected continuously are deployed here. The shipborne radar images were acquired during the oil spill monitoring cruise of the teaching-practice ship *Yukun* of Dalian Maritime University on July 21, 2010. Data collection location was the adjacent sea region of Dalian Port. The shipborne radar operated at X-band horizontal polarization. The detection range of the images was 0.75 nautical mile (NM). Radar data acquisition cycle was 2 s. The size of the images was 1024×1024 pixels.

Methods of data preprocessing

The data preprocessing flow is shown in Fig. 2. Firstly, the original images were transformed from polar coordinate system to Cartesian coordinate system. Then, the co-frequency interference noises were segmented by using improved Sobel operator convolution and Otsu threshold. The co-frequency interference noises were suppressed by linear interpolation. Next, the GICM was applied to adjust the ocean wave pixels. Because the oil film has relatively dark image characteristic, the highlight targets, especially in the oil film area, may hinder the result of image recognition. Therefore, the highlighted targets should be removed in the preprocessing. The dual-threshold method was utilized to extract the highlighted targets. Finally, the linear interpolation was employed to smooth these pixels to get the preprocessed image.

Improved Sobel operator

The Sobel operator consists of horizontal G_x and vertical G_y:

$$\begin{aligned} G_x = {} & f(x+1,y-1) + 2f(x+1,y) + f(x+1,y+1) \\ & - f(x-1,y-1) - 2f(x-1,y) - f(x-1,y+1), \end{aligned} \tag{1}$$

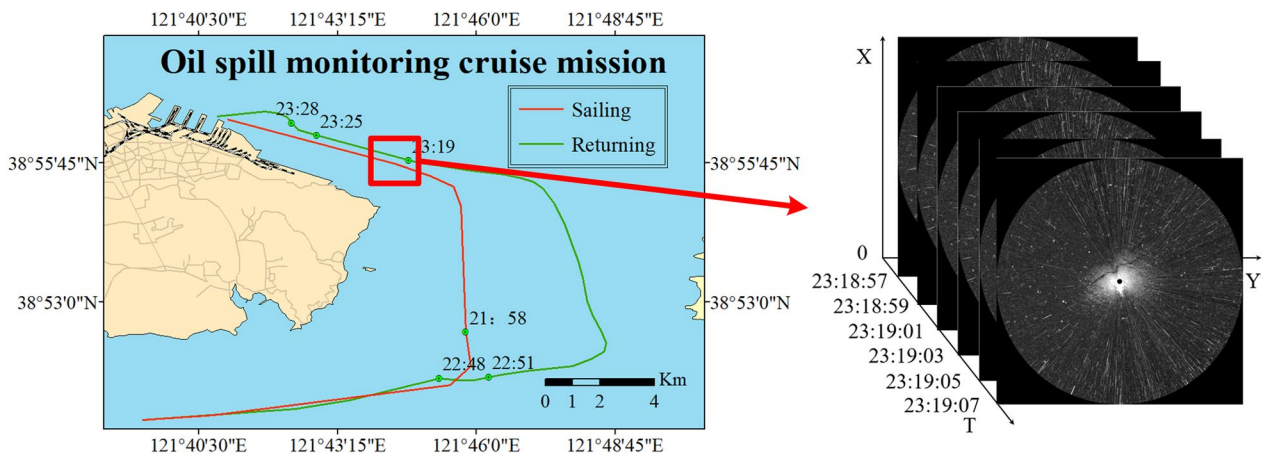

Fig. 1 Oil spill positions observed by the teaching-training ship *Yukun* on July 21, 2010

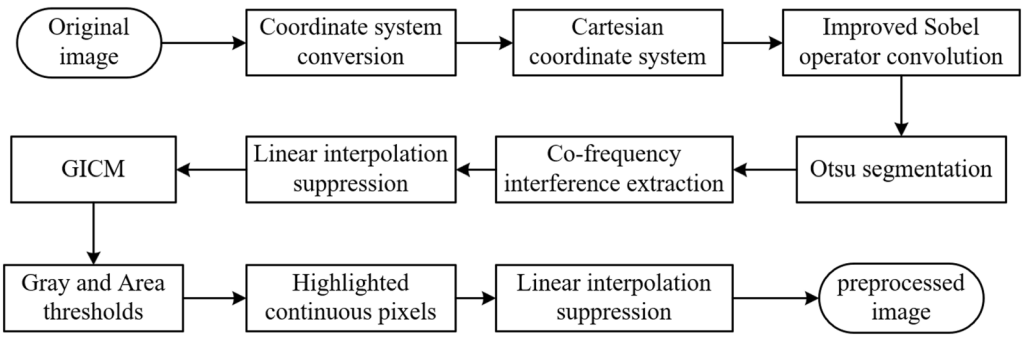

Fig. 2 Data preprocessing procedures

$$G_y = f(x-1,y-1) + 2f(x,y-1) + f(x+1,y-1) - f(x-1,y+1) - 2f(x,y+1) - f(x+1,y+1). \quad (2)$$

The G_y was improved here to highlight the co-frequency interferences and weaken other pixels as follows:

$$G_y = 2f(x,y+1) + 4f(x,y) + 2f(x,y-1) - f(x-1,y-1) - 2f(x,y-1) - f(x+1,y-1) - f(x-1,y+1) - 2f(x,y+1) - f(x+1,y+1), \quad (3)$$

where x and y are the abscissa and ordinate of the image, respectively.

Linear interpolation

Distance-weighted linear interpolation method was used to remove co-frequency interferences and highlight pixels as:

$$f(x,y) = \frac{nf(x-m,y) + mf(x+n,y)}{m+n}, \quad (4)$$

where m and n are the number of noise points on the left and right sides of the horizontal direction, respectively.

GICM

The GICM was used to adjust the gray distribution of the shipborne radar images as given in Fig. 3.

Gray and area thresholds

Continuous pixels whose gray and area met the thresholds were identified as the highlight targets H here:

$$H = \begin{cases} f(x,y) > T_{\text{gray}} \\ \text{Count(Pixels)} < T_{\text{area}} \end{cases}, \quad (5)$$

where T_{gray} and T_{area} are gray and area thresholds, respectively.

LBF model

Li et al. (2008) proposed a region-based active contour model (ACM) with a variable level set formulation that is applicable to inhomogeneous gray images. A gray image $I(x)$: $\Omega \rightarrow R$ is divided into two regions of the target R_{in} and background R_{out}, starting with a preset contour C. The LBF energy function is defined as:

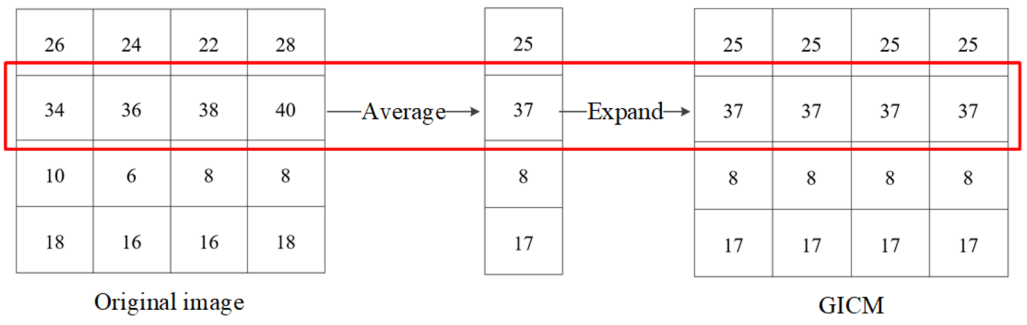

Fig. 3 Generation method of GICM

$$\varepsilon^{\mathrm{LBF}}(C,f_1(x),f_2(x)) = \lambda_1 \int_{R_{\mathrm{in}}} K(x-y)|I(x)-C_{\mathrm{in}}|^2 \mathrm{d}x + \lambda_2 \int_{R_{\mathrm{out}}} K(x-y)|I(x)-C_{\mathrm{out}}|^2 \mathrm{d}x, \quad (6)$$

where λ_1 and λ_2 are previously defined. C_{in} and C_{out} are constants that approximate image intensity of R_{in} and R_{out}, respectively. $f_1(x)$ and $f_2(x)$ are spatially varying fitting functions. Furthermore, $I(x)$ is the pixels in a window around y, while K is a kernel function with the localization property of $K(u)$ decreases and approaches zero as $|u|$ increases. A Gaussian kernel is chosen as $K(x)$ with a standard deviation of σ into the ACM:

$$K_\sigma(x) = \frac{1}{(2\pi)^{n/2}\sigma^n} e^{-|x|^2/2\sigma^2}. \quad (7)$$

Due to the localization property of $K(u)$, the contribution of $I(x)$ to the LBF energy decreases to zero as y moves away from the center point x. This property helps handle inhomogeneous gray images.

Xu et al. (2019a, b) proposed an improved LBF model with area threshold parameters for suitable target segmentation in shipborne radar images as follows:

$$D(x) = \begin{cases} A(R_{\mathrm{out}}) < T_{\mathrm{out}} \\ A(R_{\mathrm{in}}) < T_{\mathrm{in}} \end{cases}, \quad (8)$$

where A is the area of continuous pixels, T_{in} and T_{out} are the area thresholds of R_{in} and R_{out}, respectively. This improved LBF model can segment oil film contour accurately for generating centroid. It was used here to extract suspected oil spills.

Data fusion of shipborne radar image and electronic chart

The location and frequency of suspected oil spill centroids were used to discriminate the result. Xu et al. (2020a, b) proposed a target fusion method of shipborne radar and Electronic Navigation Chart (ENC). According to this method, we mapped the suspected oil spills into the ENC and extracted their centroids.

From the image matrix coordinates (X_{Pic}, Y_{Pic}) of the target, radar detection distance D, image radius R and plane coordinates of the ship (X_{os}, Y_{os}), the plane coordinates (X_p, Y_p) of the target contour boundary points can be obtained as:

$$\begin{cases} X_p = X_{\mathrm{os}} + (X_{\mathrm{Pic}}/R)D \\ Y_p = Y_{\mathrm{os}} + (Y_{\mathrm{Pic}}/R)D \end{cases}. \quad (9)$$

Based on GIS technology, target contour boundary points are converted back orderly to the geographic coordinates of the WGS_1984 coordinate system. The target polygons and their centroids can be generated on ENC.

Oil spill discrimination mechanism

Oil spill discrimination mechanism (Fig. 4) was designed as follows:

a. Taking the suspected oil spill centroid detected for the first time as the center, new suspected oil film centroids are retrieved in the following images with the distance threshold T_{dis} in the time threshold T_{time} for statistical quantity (including suspected oil film centroids as the center and new suspected oil film centroids retrieved).

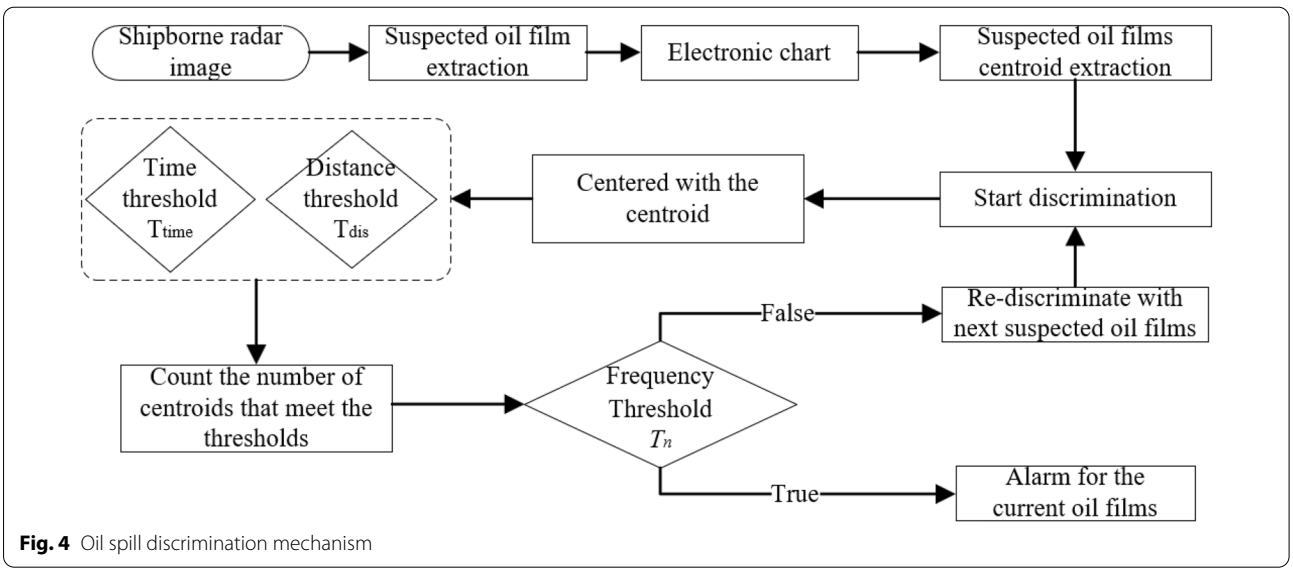

Fig. 4 Oil spill discrimination mechanism

b. When the number of centroids retrieved reaches the frequency threshold T_n, it is judged that oil spills exist, and the alarm is given. Otherwise, the suspected oil film centroid detected for the next time will be taken as the center for re-judgement.

The T_{time} is related to the motion state of the ship. The ideal setting of the T_{time} is the total time of 5 image acquisition cycles before the ship leaves the region of the suspected oil film detected. If the shipborne radar is installed on the shore or the ship is berthing at the anchorage, the T_{time} can be completely set as 5 shipborne radar image acquisition cycles. The T_{dis} is set to 1/12 of the radar image detection range by default. For example, for a shipborne radar image with a detection range of '3' NM, the T_{dis} is set to '0.25' NM. The recommended value of the T_n is 4/5 of the number of image acquisition cycles of the T_{time}. If the T_{time} is set to the total time of 5 image acquisition cycles, then the T_n is recommended as '4'.

Results

Data preprocessing

The image, in which suspected oil films appeared at the first time (image collected at 23:18:56), was used for describing the data preprocessing, as shown in Fig. 5a. The shipborne radar image in Cartesian coordinate system retains useful vertical image features. For example, as the distance becomes longer, the gray value of the sea wave pixels decreases. This image feature is more obvious in Cartesian coordinate system. The co-frequency interferences only show as vertical linear noises in Cartesian coordinate system. Therefore, the image was firstly transformed from polar coordinate system to Cartesian coordinate system as in Fig. 5b. After the improved Sobel operator convolution and Otsu threshold segmentation, the co-frequency interferences and highlighted independent pixels were extracted, as shown in Fig. 5c. The white pixels in Fig. 5c were suppressed by linear interpolation as Fig. 5d.

The GICM model of Fig. 5d was generated as Fig. 6a. The subtraction of Fig. 5d and its GICM model was applied to adjust the image gray distribution as in Fig. 6b. After that, gray and area thresholds were used to get the highlighted targets as in Fig. 6c. Linear interpolation was employed to smooth them as in Fig. 6d. Finally, the preprocessed image was converted to polar coordinate system as Fig. 6e, f.

Suspected oil slick extraction

An improved LBF model was used to extract suspected oil films in shipborne radar images here. The window size of Gauss kernel was 13×13, $\sigma = 3$, $\lambda_1 = 1$, $\lambda_2 = 2$, i (iterations) $= 40$, $T_{\text{in}} = 20$, and $T_{\text{out}} = 10$. Because the results of the improved LBF model needed to be integrated into the north-up ENC to generate the centroids of suspected oil films, it was necessary to rotate the extracted suspected oil films by the azimuth as Fig. 7. The heading azimuth of the image was '70.1°'.

Extraction of suspected oil film centroids

A target fusion method of shipborne radar image and ENC was used to integrate the suspected oil films into ENC based on ArcGIS Engine. The centroid (Fig. 8) of the suspected oil films and its WGS-1984 geographical coordinates were extracted by using the *Centroid* attribute of the *IArea* interface. After that, geographic coordinates were transformed to Beijing-1954 coordinates by projection transformation as Table 1. Simultaneously, the area detected of oil films in the images could be obtained by using the *Area* attribute of the *IArea* interface.

Disrimination of oil spill

Set $T_{\text{time}} = 10$ s, $T_{\text{dis}} = (0.75 \text{ NM} \times 1852 \text{ M/NM}) \div 12 = 115.75$ M, $T_n = 4$. Calculate the distances between Centroid 1 and the other Centroids as Table 2 in succession. Count the number when the distances between Centroid 1 and other centroids are less than T_{dis}. When the number reached T_n, end calculation and determine the suspected oil films of Centroid 1 as true. If the number did not reach T_n, they would be judged as false oil films.

Discussion

Limitations of proposed multi-time-domain shipborne radar oil spill discrimination

Limitations of proposed multi-time-domain shipborne radar oil spill discrimination includes:

a. Shipborne radar oil spill monitoring information comes from the echo images of ocean surface. If the wave echoes became weak, it would be difficult to detect the oil films.
b. For the same oil films, the monitoring results might be various in different shipborne radar images because the whole oil films did not com-

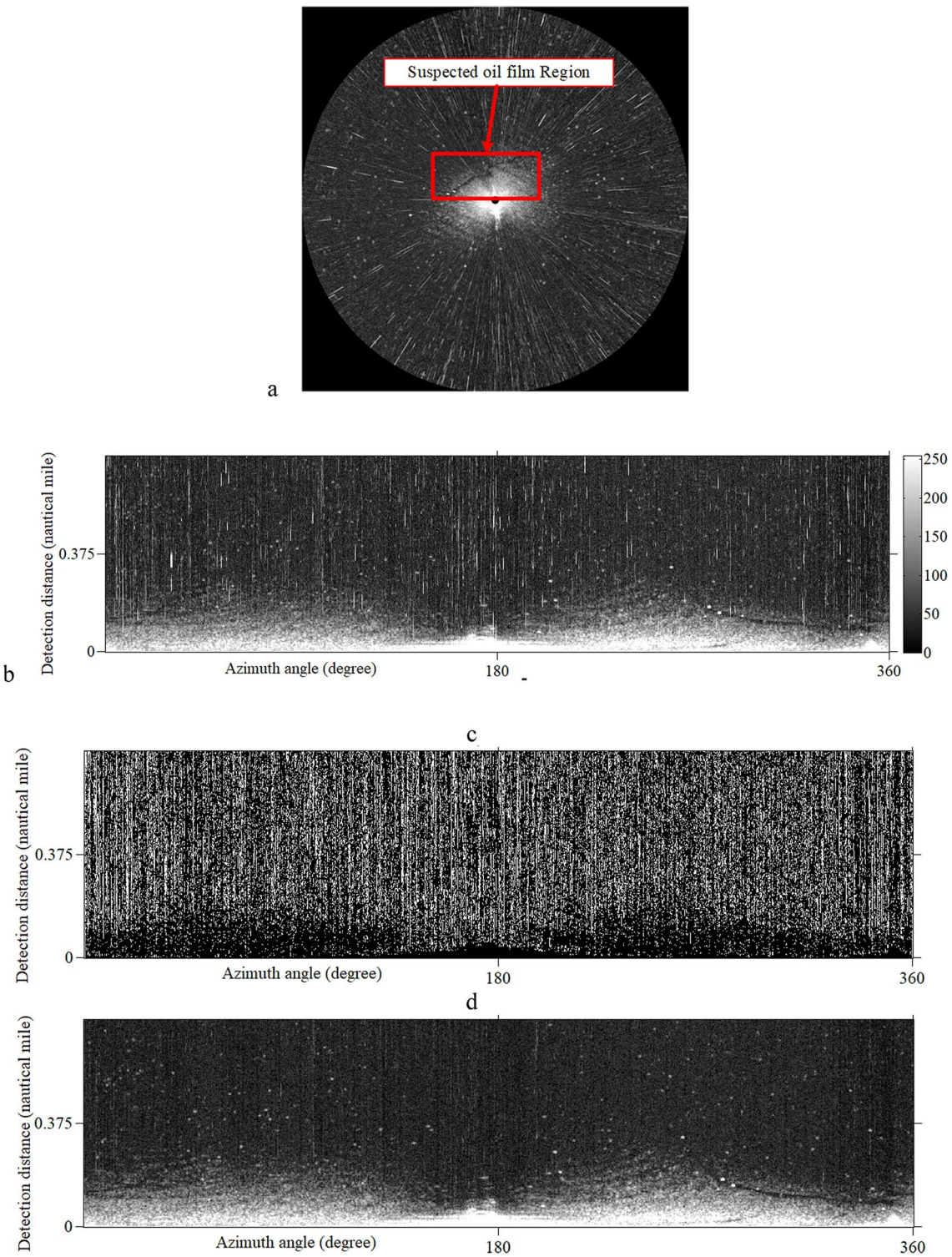

Fig. 5 The suppression of the co-frequency interferences and independent highlight pixels. **a** Suspected oil spills appeared at the first time; **b** Cartesian coordinate system transformation; **c** improved Sobel operator convolution and Otsu threshold segmentation, **d** linear interpolation suppression

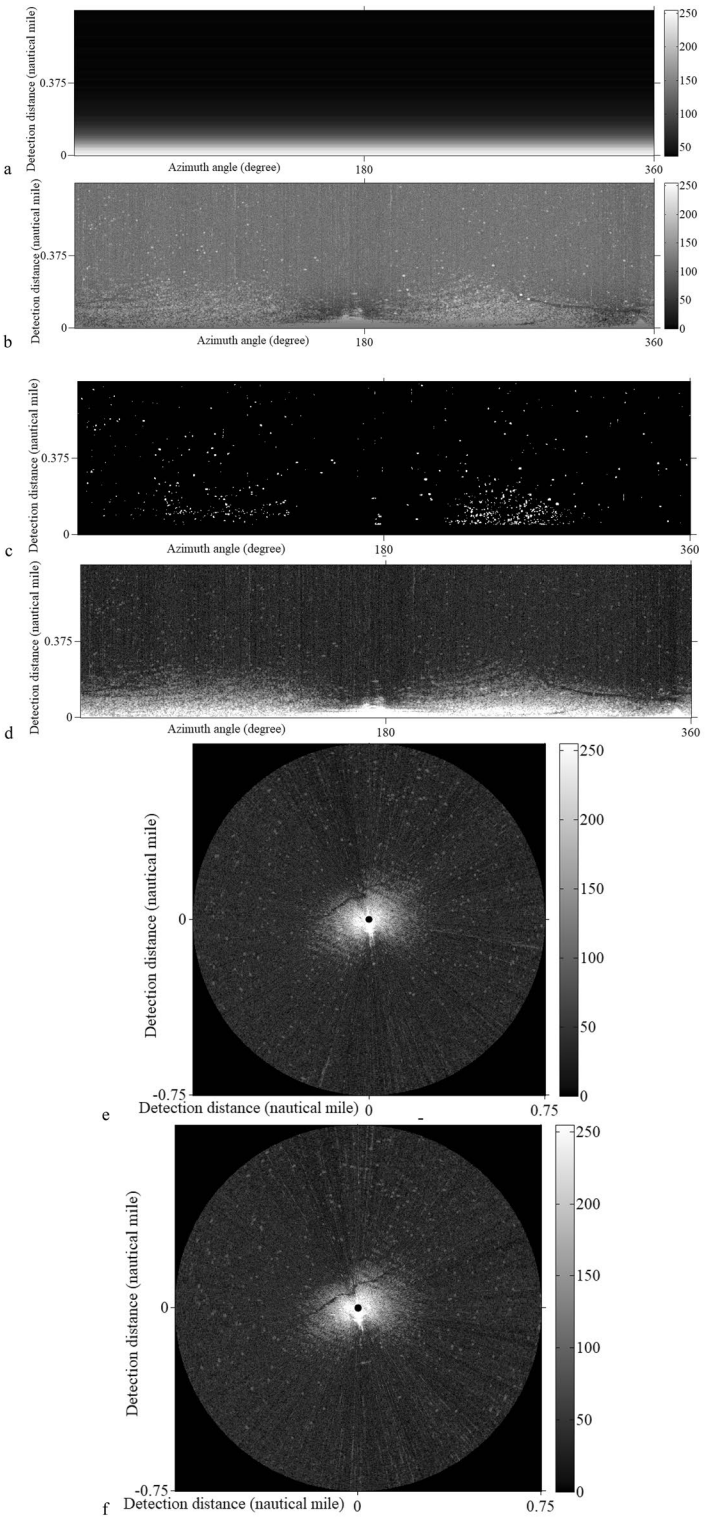

Fig. 6 Data preprocessing results. **a** GICM model of Fig. 5d; **b** subtraction of Fig. 5d and **a**. **c** Highlighted targets segmentation by using gray threshold (160) and area threshold (100); **d** linear interpolation suppression; **e**, **f** are the preprocessed results of images collected at 23:18:56 and 23:19:07, respectively

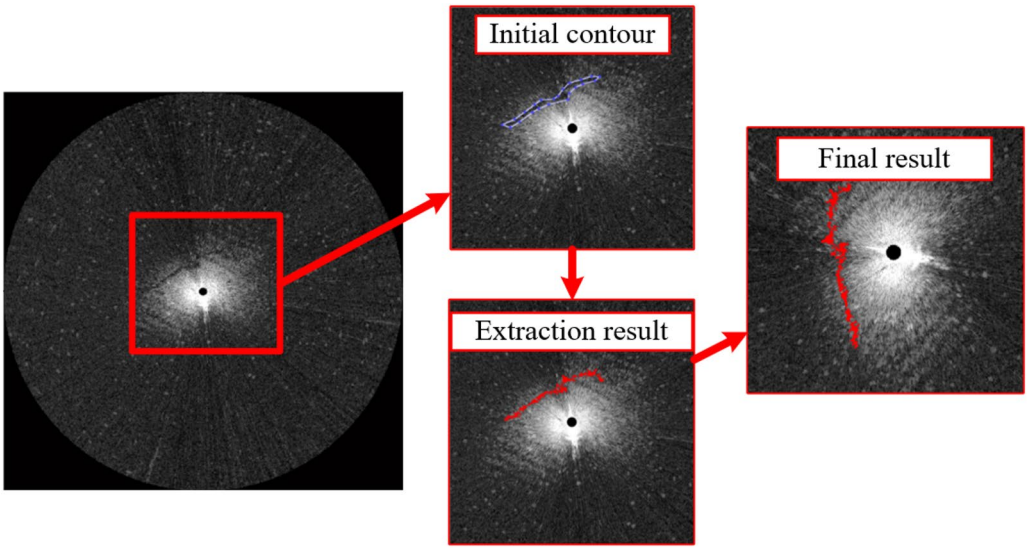

Fig. 7 Suspected oil films extraction by an improved LBF

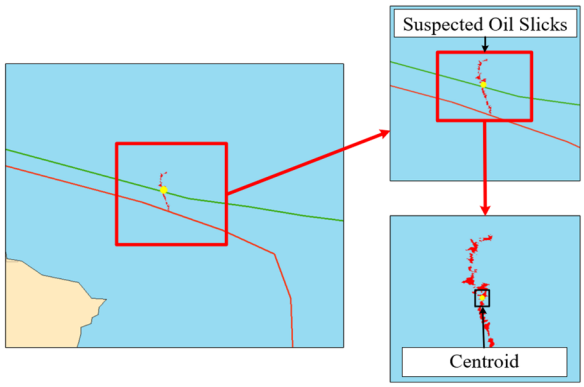

Fig. 8 Centroid extraction of suspected oil films

Table 1 Centroids Beijing-1954 coordinates of suspected oil films

ID	*X* (M)	*Y* (M)	Area (M^2)
1	391,021.49	4,311,618.38	9218.12
2	391,017.67	4,311,562.87	6373.57
3	391,010.76	4,311,587.78	9424.19
4	391,007.59	4,311,585.22	9100.36
5	391,010.67	4,311,553.12	7348.74
6	391,005.40	4,311,561.83	8117.83

Table 2 Distances between Centroid 1 and the other centroids

Centroid ID	Distance (M)
1–2	55.64
1–3	32.43
1–4	35.96
1–5	66.15
1–6	58.79

pletely enter the monitoring region due to the ship motion. For example, the monitoring regions of the same oil films in centroids 1 and 2 of Table 1 were different. Therefore, it was more appropriate to describe as "monitored oil films".

c. In the process of extracting suspected oil films, in order to get the profiles of oil films, an improved LBF model was used here for result segmentation which needed to set the initial contour. The preset contour increased the system consumption of image analysis. In the future, the rapid and automatic oil spill identification method should be developed to improve the efficiency. Meanwhile, improving the speed of image acquisition can also contribute to quick warning.

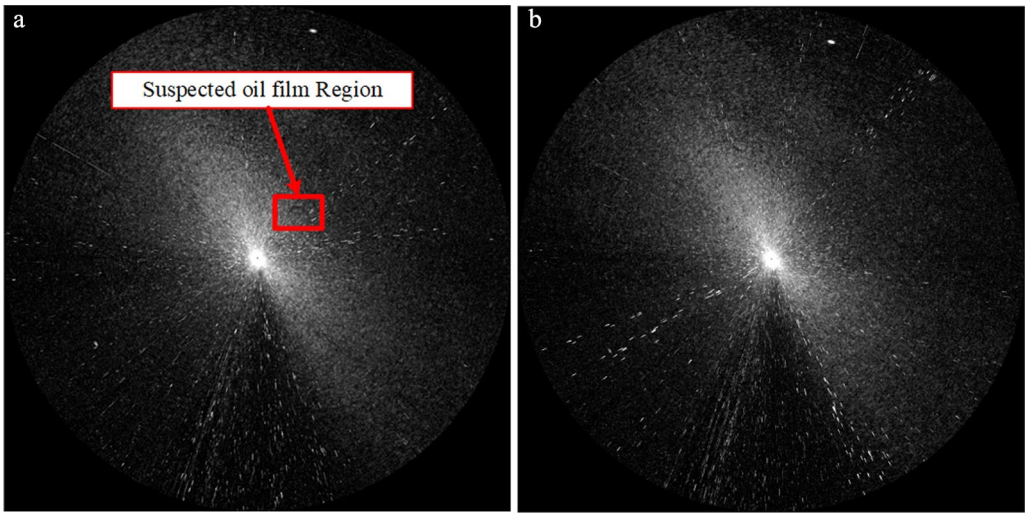

Fig. 9 Discrimination of unreal oil spills. **a**, **b** Were collected at 14:07:50 and 14:08:19 on August 12, 2015, respectively. **a** Suspected oil films appeared at the first time; **b** suspected oil films disappeared in the next image

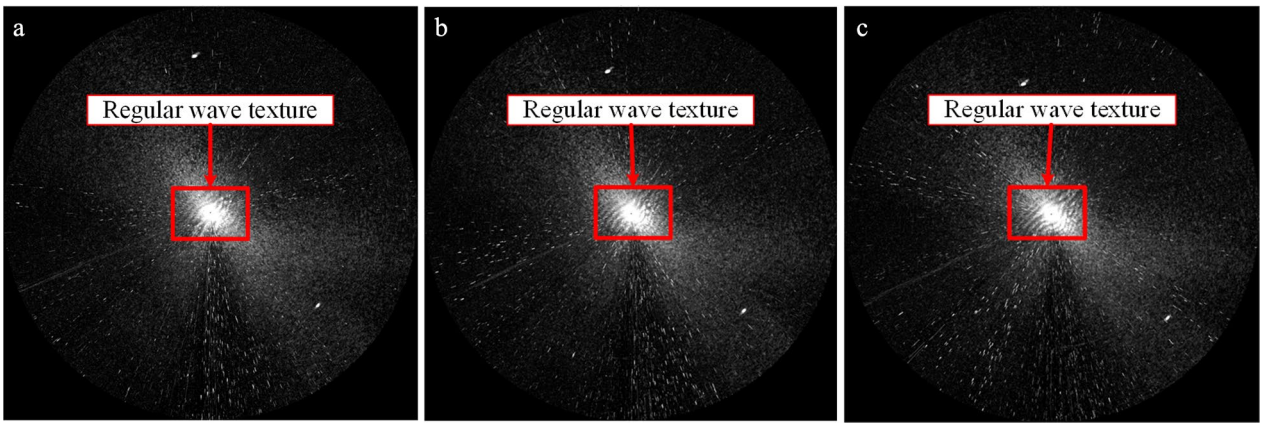

Fig. 10 Regular wave texture images with suspected oil film features. **a**–**c** Were collected at 14:51:19, 14:51:50 and 14:52:19 on August 12, 2015, respectively

Discrimination of false oil films

T_{time} and T_{dis} are the filters of our discrimination mechanism. T_n is the key. For 6 consecutive images, 4 images with the same oil films were the basis to determine the existence of oil films. Figure 9 contains two consecutive shipborne radar images. The suspected oil films appeared at the first time in Fig. 9a, but the second image (Fig. 9b) non-existed the same suspected oil films. This situation was judged as non-oil-spill, and no alarm was given. The regular wave near the ship showed suspected oil films features occasionally, but not the real oil spills, as shown in Fig. 10. If this happened in the daytime, the possibility of oil spills could be judged by visual observation or visible light images as in Fig. 11a. Data of infrared or laser fluorescence could be applied to help identification during the night. Our experimental images were collected at night, and the thermal infrared image (Fig. 11b) was obtained at the same time. Oil films have somewhat lower gray values than water in

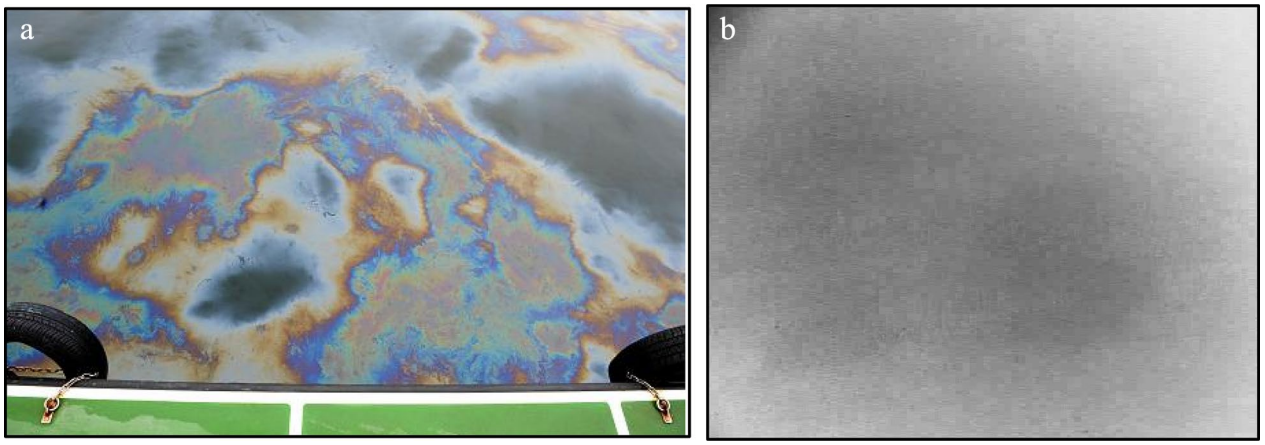

Fig. 11 Oil spill auxiliary identification methods of shipborne radar. **a** The oil films during the daytime was photographed on July 19, 2010. **b** Infrared image of sea surface at night of 716 oil spill accident

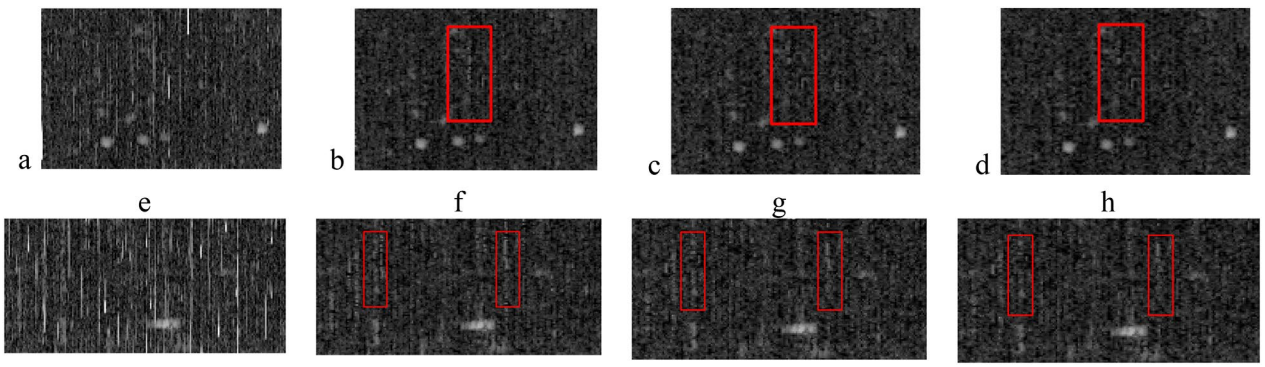

Fig. 12 Noise reduction results of co-frequency interferences. **a**, **b** Were the (100:200, 320:470) and (320:410, 880:1070) of Fig. 5b. **b**, **f** Were the results of the Laplace operator. **c**, **g** Were the results of an improved Prewitt operator. **d**, **h** Were the results of our improved Sobel operator

Table 3 Evaluation results of three operators for detecting co-frequency interferences

Operator	SNR	PSNR	SSIM
Laplace	6.4648	20.8660	0.6836
Improved Prewitt	5.6144	20.8473	0.6943
Improved Sobel	5.0662	20.5543	0.6598

thermal infrared images (Fingas and Brown 2014). The thermal infrared image also shows suspected oil films feature, which proved the reliability of shipborne radar oil spill detection.

Comparison of detection operators for co-frequency interference

The Laplace operator and an improved Prewitt operator were used to detect co-frequency interferences in the shipborne radar images (Xu et al. 2018; Xu et al. 2019a, b). The Laplace operator is:

$$\nabla^2 f_1(x,y) = 4f(x,y) - f(x+1,y) - f(x-1,y) - f(x,y+1) - f(x,y-1). \quad (10)$$

The improved Prewitt operator is:

$$G'(i,j) = 2f(i-1,j) + 2f(i+1,j) + 2f(i,j) - f(i-1,j-1) - f(i,j-1) \quad - f(i+1,j-1) - f(i-1,j+1) - f(i,j+1) - f(i+1,j+1). \quad (11)$$

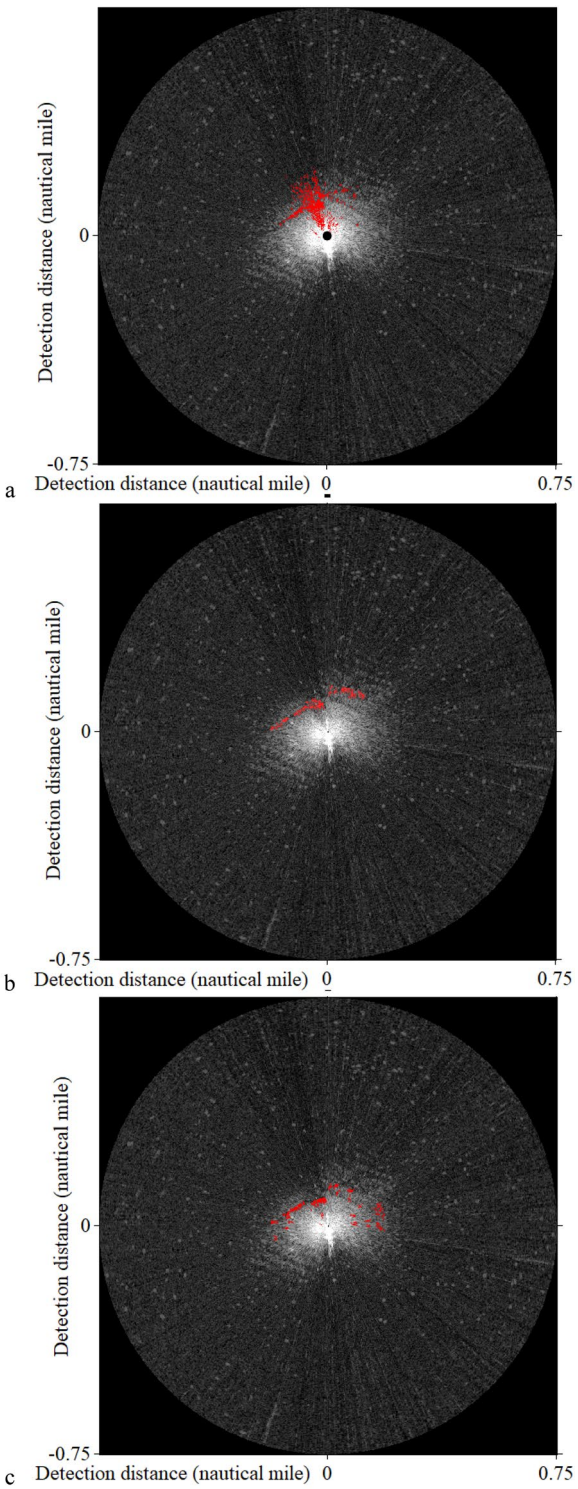

Fig. 13 Segmentation results of suspected oil films of other three methods. **a** Manual threshold method; **b** dual-threshold method; **c** adaptive threshold method

The two operators were used to compare with our improved Sobel operator for detecting co-frequency interferences of Fig. 5b as Fig. 12. The results show that the Laplace operator had the worst noise detection ability, the improved Prewitt operator performed better, and our improved Sobel operator had the best effect. The signal-to-noise ratio (SNR), peak signal-to-noise ratio (PSNR) and structural similarity (SSIM) were used as evaluation indicators after Otsu segmentation and linear interpolation as Table 3. From the three indicators, the Laplace operator and the improved Prewitt operator had higher values, and our improved Sobel operator had a lower value, which proved that the improved Sobel operator can detect more co-frequency interference noises and effectively suppress them. To sum up, our improved Sobel operator was more suitable for the detection of co-frequency interference in the shipborne radar original images.

Comparison with existing methods of shipborne radar oil spill detection

Manual threshold method (Zhu et al. 2015), dual-threshold method (Xu et al. 2018) and adaptive threshold method (Xu et al. 2019a, b) were used to segment suspected oil spills for comparison. The above three methods were used in our shipborne radar image as Fig. 13. According to our pretreatment method, the results of manual threshold method and dual-threshold method missed some suspected oil films. The adaptive threshold method result appeared more false suspected oil films. Compared with the above three methods, the improved LBF model used here can segment the suspected oil films more accurately in the light of results of Figs. 7 and 13. Dual-threshold method and adaptive threshold method needed to determine the effective monitoring range of oil spills by the gray distribution matrix (Fig. 14). This matrix needed many tests to find the appropriate gray threshold under different sea conditions. In terms of calculation time, manual threshold method, dual-threshold method and adaptive threshold method took 1.76 s, 3.04 s and 3.69 s, respectively. After 20 iterations, the improved LBF model took 9.25 s. The disadvantage of LBF model used here is how to automatically select appropriate preset contour for oil films segmentation. Quick and automatic acquisition method of accurate suspected oil films is the most important breakthrough in our future work.

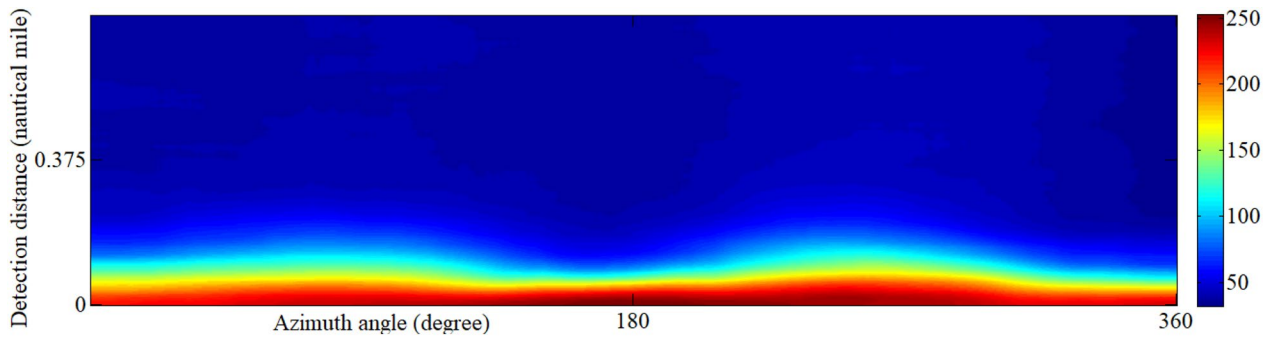

Fig. 14 The gray distribution matrix of Fig. 5b

Conclusions

Oil spill monitoring technology has become a hot spot in remote sensing. The application of shipborne radar in this field is still in its infancy, but has broad application value and promotion prospects. At first, we proposed a new image preprocessing scheme for shipborne radar oil spill detection. This paper focuses on an oil film discrimination mechanism based on multi-time-domain images to reduce the false alarm rate, so as to ensure the effective response to oil spill emergency disposal.

Acknowledgements

The authors of this research would like to thank all the field management staff at the teaching-training ship *Yukun* during our research.

Authors' contributions

JX conceived and performed the experiments; XXP planned the experiments and revised the manuscript; XRW and BZJ revised the manuscript; HW and CC collected data and helped perform the analysis with constructive discussions; BL and JF contributed to revisions and approved the final version. All authors have agreed to the published version of the manuscript. All authors read and approved the final manuscript.

Funding

This work was supported by the National Natural Science Foundation of China, Grant Numbers 51709031 and 51979045; the Fundamental Research Funds for the Central Universities, Grant Number 3132019138; the Innovation Support Project of Dalian, Grant Number 2018RQ22; the Enterprise-university-research Cooperation Project of the Ministry of Education of China, Grant Number 201702043016, the Special projects in key fields (Artificial Intelligence) of Universities in Guangdong Province, Grant Number 2019KZDZX1035; the program for Scientific Research Start-up Funds of Guangdong Ocean University.

Availability of data and materials

The experimental data are shipborne radar images collected by Dalian Maritime University, which are not open to the public.

Declarations

Competing interests

The authors declare that they have no competing interests.

Author details

[1] Maritime College, Guangdong Ocean University, Zhanjiang, Guangdong, China. [2] School of Resources, Environment and Architectural Engineering, Chifeng University, Chifeng, Inner Mongolia, China. [3] Shanghai Astronomical Observatory, Chinese Academy of Sciences, Shanghai, China. [4] Shanghai Key Laboratory of Space Navigation and Positioning Techniques, Shanghai, China. [5] Information Engineering College, Lingnan Normal University, Zhanjiang, Guangdong, China. [6] Navigation College, Dalian Maritime University, Dalian, Liaoning, China. [7] Continuing Education College, Guangdong Ocean University, Zhanjiang, Guangdong, China. [8] Civil Aviation College, Shenyang Aerospace University, Shenyang, Liaoning, China.

Received: 14 September 2020 Accepted: 27 February 2021
Published online: 07 March 2021

References

Atanassov V, Mladenov L, Rangelov R, Savchenko A (1991) Observation of oil slicks on the sea surface by using marine navigation radar. Proc IGARSS. https://doi.org/10.1109/IGARSS.1991.579326

Chen T, Lu SJ (2017) Subcategory-aware feature selection and SVM optimization for automatic aerial image-based oil spill inspection. IEEE Trans Geosci Remote Sens 55(9):5264–5273

Chen YT, Li YY, Wang JS (2010) An end-to-end oil-spill monitoring method for multisensory satellite images based on deep semantic segmentation. Sensors 20(3):725. https://doi.org/10.3390/s20030725

Colvin KA, Lewis C, Galloway TS (2020) Current issues confounding the rapid toxicological assessment of oil spills. Chemosphere 245:125585. https://doi.org/10.1016/j.chemosphere.2019.125585

Eronat AH (2020) Time series evaluation of oil spill in marine environment: a case study in marine area of Cyprus. Arab J Geosci 13(10):365. https://doi.org/10.1007/s12517-020-05388-6

Fingas M, Brown CE (2014) Review of oil spill remote sensing. Mar Pollut Bull 83(1):9–23. https://doi.org/10.1016/j.marpolbul.2014.03.059

Li CM, Kao CY, Gore JC, Ding Z (2008) Minimization of region scalable fitting energy for image segmentation. IEEE Trans Image Process 17(10):1940–1949. https://doi.org/10.1109/TIP.2008.2002304

Li Y, Lu HM, Zhang ZD, Liu P (2020) A novel nonlinear hyperspectral unmixing approach for images of oil spills at sea. Int J Remote Sens 41(12):4682–4699. https://doi.org/10.1080/01431161.2020.1723179

Liu BX, Li Y, Li GN, Liu A (2019a) A spectral feature based convolutional neural network for classification of sea surface oil spill. ISPRS Int J Geo-Inf 8(4):160. https://doi.org/10.3390/ijgi8040160

Liu P, Li Y, Xu J, Wang T (2019b) Oil spill extraction by X-band marine radar using texture analysis and adaptive thresholding. Remote Sens Lett 10(6):583–589. https://doi.org/10.1080/2150704X.2019.1587197

Maamar A, Lucchesi ME, Debaets S, van Long NN, Quemener M, Coton E, Bouderbala M, Burgaud G, Matallah-Boutiba A (2020) Highlighting the crude oil bioremediation potential of marine Fungi isolated from the Port of Oran (Algeria). Diversity 12(5):196. https://doi.org/10.3390/d12050196

Magris RA, Giarrizzo T (2020) Mysterious oil spill in the Atlantic Ocean threatens marine biodiversity and local people in Brazil. Mar Pollut Bull 153:110961. https://doi.org/10.1016/j.marpolbul.2020.110961

Novelli G, Guigand CM, Boufadel MC, Ozgokmen TM (2020) On the transport and landfall of marine oil spills, laboratory and field observations.

Mar Pollut Bull 150:110805. https://doi.org/10.1016/j.marpolbul.2019.110805
Soares MD, Teixeira CEP, Bezerra LEA, Paiva SV, Tavares TCL, Garcia TM, de Araujo JT, Campos CC, Ferreira SMC, Matthews-Cascon H, Frota A, Mont'Alverne TCF, Silva ST, Rabelo EF, Barroso CX, de Freitas JEP, de Melo M, Campelo RPD, de Santana CS, Carneiro PBD, Meirelles AJ, Santos BA, de Oliveira AHB, Horta P, Cavalcante RM (2020) Oil spill in South Atlantic (Brazil): environmental and governmental disaster. Mar Policy 15:103879. https://doi.org/10.1016/j.marpol.2020.103879
Tennyson EJ (1988) Shipboard navigational radar as an oil spill tracking tool—a preliminary assessment. Proc OCEANS. https://doi.org/10.1109/OCEANS.1988.23623
U.S. District Court for the Eastern District of Louisiana (2010) Findings of fact and conclusions of law phase two trial. The United States District Court for the Eastern District of Louisiana, Louisiana
Vickner SS (2020) On estimating the impact of the deepwater horizon tragedy on the US frozen seafood market: a conditional almost ideal demand system approach. Sustainability 12(10):4191. https://doi.org/10.3390/su12104191
Villalonga MM, Infantes ME, Colls MG, Ridge MM (2020) Environmental management system for the analysis of oil spill risk using probabilistic simulations. Application at Tarragona Monobuoy. J Mar Sci Eng 8(4):277. https://doi.org/10.3390/jmse8040277
Xu J, Liu P, Wang HX, Lian JJ, Li B (2018) Marine radar oil spill monitoring technology based on dual-threshold and C-V level set methods. J Indian Soc Remote Sens 46(12):1949–1961. https://doi.org/10.1007/s12524-018-0853-4
Xu J, Cui C, Feng HY, You DM, Wang HX, Li B (2019a) Marine radar oil spill monitoring through local adaptive thresholding. Environ Forensics 20(2):196–209. https://doi.org/10.1080/15275922.2019.1597781
Xu J, Wang H, Cui C, Liu P, Zhao Y, Li B (2019b) Oil spill segmentation in shipborne radar images with an improved active contour model. Remote Sens 1(14):1698. https://doi.org/10.3390/rs11141698
Xu J, Jia BZ, Pan XX, Li RH, Cao L, Cui C, Wang HX, Li B (2020a) Hydrographic data inspection and disaster monitoring using shipborne radar small range images with electronic navigation chart. PeerJ Comput Sci. https://doi.org/10.7717/peerj-cs.290
Xu J, Wang HX, Cui C, Zhao BG, Li B (2020b) Oil spill monitoring of shipborne radar image features using SVM and local adaptive threshold. Algorithms 13(3):69. https://doi.org/10.3390/a13030069
Ye XD, Chen B, Lee K, Storesund R, Zhang BY (2020) An integrated offshore oil spill response decision making approach by human factor analysis and fuzzy preference evaluation. Environ Pollut 262:114294. https://doi.org/10.1016/j.envpol.2020.114294
Yim UH, Khim JS, Kim M, Jung JH, Shim WJ (2017) Environmental impacts and recovery after the Hebei Spirit oil spill in Korea. Arch Environ Con Tox 73(1):47–54
Yuan LL, Han LX, Chen Q, Zhang Y, Chen B (2020) Simulation for dynamic release of oil from oil-contaminated marine sediment. Environ Sci Pollut Res 27(14):16841–16852. https://doi.org/10.1007/s11356-020-08239-9
Zeng K, Wang Y (2020) A deep convolutional neural network for oil spill detection from spaceborne SAR images. Remote Sens 12(6):1015
Zhang J, Feng H, Luo Q, Li Y, Wei J, Li J (2020) Oil spill detection in quad-polarimetric SAR images using an advanced convolutional neural network based on super pixel model. Remote Sens 12(6):944
Zhou Y, Lu YC, Shen YF, Ding J, Zhang MW, Mao ZH (2020) Polarized remote inversion of the refractive index of marine spilled oil from PARASOL images under sun glint. IEEE Trans Geosci Remote Sens 58(4):2710–2719. https://doi.org/10.1109/TGRS.2019.2953640
Zhu X, Li Y, Feng H, Liu B, Xu J (2015) Oil spill detection method using X-band marine radar imagery. J Appl Remote Sens 9(1):095985. https://doi.org/10.1117/1.JRS.9.095985

Publisher's Note